Mechanics & Industry **21**, 112 (2020)
© AFM, EDP Sciences 2020
https://doi.org/10.1051/meca/2019090

Mechanics & Industry

Available online at:
www.mechanics-industry.org

Regular Article

# The non-isothermal hot deep drawing of AA5083 aluminum alloy

Abozar Barimani Varandi*

Department of Mechanical Engineering, Babol Noshirvani University of Technology, Babol, Mazandaran Province, Iran

Received: 21 February 2019 / Accepted: 9 August 2019

**Abstract.** The present work is focused on the hot deep drawing process for cylindrical 5083 aluminum alloy parts, by superimposing a thermal gradient between the blank center-flange region. The imprtance of application of forming processes at elevated temperatures, in improving the formability, has increasingly attracted attention in recent years. As a case study, the experimental and numerical tests were performed at three speeds (60, 200 and 378 mm $min^{-1}$) from room temperature (RT) up to 0.9 melting point, inspired by the advent of extraordinary superplastic behavior of AA5083 in hot condition. In particular, the focus was on the effects of forming speed on punch load, thickness distribution, and earing behavior. Finite element simulations were run in order to investigate the limiting drawing ratio and temperature gradient. The tests highlight that by increasing the temperature, the number and the position of the ears are constant, while the height of ears decreases. Furthermore, limiting drawing ratio equal to 2.84 is reached at 550 °C.

**Keywords:** Aluminum alloy / forming speed / forming temperature / non-isothermal / hot deep drawing

## 1 Introduction

In recent decades, interests in aluminum alloys have progressively increased in aerospace, automotive, and electronic industries due to their lightweight and high specific strength properties. The application of lightweight materials including aluminum and magnesium alloys is limited due to their low formability at room temperature (RT). Many researches pointed out that the aluminum alloys, especially the 5000, 6000, and 7000 series, as well as AZ31 and AZ61 magnesium alloys are characterized by good formability at elevated temperatures. These results led to the rising trend of utilizing warm forming processes [1].

Deep drawing is one of the most widely used sheet metal forming processes, which involves various process parameters [2,3]. Many researches are carried out on deep drawing process in warm condition because of its role on formability enhancement. Naka et al. [4] studied the deep drawability of AA5083 at different temperatures in non-isothermal conditions. They obtained higher drawing ratios at elevated temperatures. Moon et al. [5] performed experiments to control the temperature of the tool aiming to increase the deep drawability of the 1050 aluminum, and reported that drawability has a high sensitivity to the temperature of the matrix and the punch. They showed that controlling the temperature of the tool is a very effective measure to improve the drawability of AA1050. Naka et al. [6], in another study, determined the forming limit diagrams for AA5083 using stretch forming experiments, with a hot punch at different speeds and temperatures. Takuda et al. [7] investigated the formability of AA5182 using non-isothermal warm deep drawing process. They showed that at elevated temperatures, the forming limit depends on the fracture close to the corner radius of matrix cavity, and the drawing ratio increases by rising of this factor. Wang et al. [8] observed that deep drawability and stretchability for AA7075 significantly increased via heating to 140–220 °C. However, the formability decreased at temperatures above 260 °C. Chu et al. [9] investigated the formability of 5086 aluminum at various temperatures and strain rates using Marciniak test setup. They reported that the formability rises and reduces respectively with the increase in temperature and speed. Two different aluminum alloys (6016 and 6061) were deepened at RT and 250 °C by Ghosh et al. [10], and the effect of punch speed, drawing ratio, holding time, and annealing was investigated and compared for both of the alloys. Laurent et al. [11] evaluated the deep drawability of AA5754 employing experimental and numerical tests. They reported that force-displacement changed during forming, and earring behavior and springback were heavily influenced by temperatures above 150 °C. Cetin et al. [12] conducted a research on characterization of forming temperature and experimentation to solve challenges of warm drawability of AA5754 under non-isothermal conditions. Noder et al. [13] reported a significant drop in strength for higher forming

* e-mail: barimani.abozar@gmail.com

**Table 1.** Chemical composition of AA5083 (wt.%).

| Ti | Zn | Ni | Cr | Mg | Mn | Cu | Fe | Si |
|---|---|---|---|---|---|---|---|---|
| 0.02 | 0.02 | 0.01 | 0.10 | 4.60 | 0.65 | 0.01 | 0.20 | 0.07 |

temperatures, resulted of the lower sections at two different initial blank temperatures (187 °C and 253 °C). Noder et al. [14], in another research, studied the developmental 7XXX-T76 aluminum alloy and reported a mild stress anisotropy and a planar strain anisotropy, that was obvious in the presence of eight ears in non-isothermal circular cup draws. It may be noted that to apply the thermal gradient at the blank center, the flange region is often heated by heating the matrix or blank holder, and the region in contact with the blank center is cooled down by the cooling punch [4,10,15–18].

The majority of reviewed researches for non-isothermal condition, were mainly aimed to temperatures below 350 °C. While some aluminum alloys, such as 5083 and 7075, exhibit a dramatic enhancement in formability at temperatures above 0.4 melting point and under specific condition, with the advent of superplastic behavior [19]. AA5083 is the least costly aluminum alloy that can trigger this behavior [20]. To the authors' knowledge, no experiment was conducted on non-isothermal deep drawing of AA5083 up to 0.9 melting point.

The main objective of the present study is to investigate the improvement of non-isothermal deep drawability of 5083 aluminum alloy in a range from RT up to 550 °C. Through the finite element simulation, the limiting drawing ratio (LDR) and temperature gradient are analyzed. The influences of forming speed on the punch load, thickness distribution and earring behavior are also discussed using experimental tests.

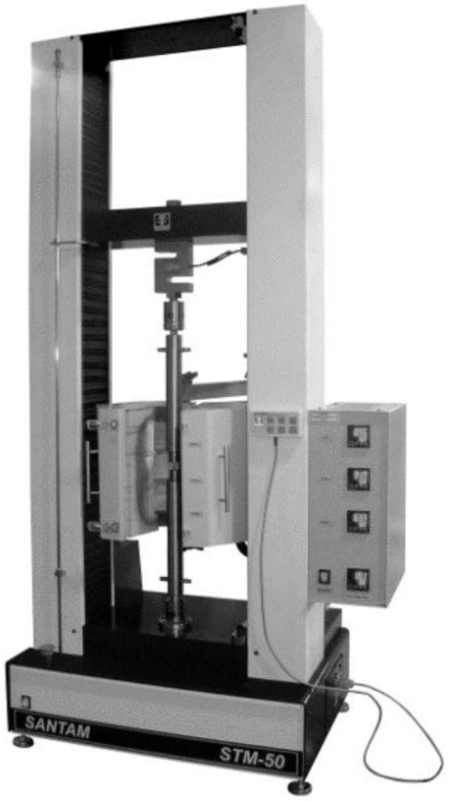


**Fig. 1.** Universal testing machine STM-50 equipped thermal furnace.

## 2 Materials and methods

### 2.1 Experimental

The 2 mm thick, aluminum alloy 5083 sheets were used with the chemical composition described in Table 1. The uniaxial drawing tests were performed according to ASTM-A370 standard until fracture occurred at different strain rates in wide temperature range. A universal testing machine STM-50 was used for the test as shown in Figure 1. The stress-strain curves are plotted in Figure 2. In addition, deep drawing tests were carried out by variable speed hydraulic press (capacity of 60 tons), with the ability to record force-displacement changes.

For experimental tests, a punch with the flat head, diameter of 36 mm, and a corner radius of 8 mm was used. The matrix had an inner cavity of 44 mm and corners with radius of 8mm. The test setup is depicted in Figure 3. In this process, the forming limit is evaluated by the LDR. The deep drawing die setup including punch, blank holder, and matrix, made of warm working steel (DIN 1.2344), were used for experiments.

The flange region of the blank was heated by a rod heater wrapping around the matrix with a power of 1.5 kW. The blank center was cooled with a water cooling punch, consisting of two input and output channels. A thermocouple was placed in contact with the bottom of the blank. After reaching the set temperature, the punch touched the blank for 10 seconds, and then the process was carried out. In Figure 4, the die setup and the equipment used for applying the temperature gradient are presented.

The blanks were prepared and lubricated at the region in contact with both blank holder and matrix, and then the initial blank holder forces were exerted. At the end of the process, the part was removed from the free end of the matrix. The LDR is calculated by the ratio of the maximum diameter of the sound formed part to the punch diameter. The experiments were carried out at three different speeds of 60, 200, and 378 mm $min^{-1}$ at different temperatures. Each test was repeated three times, and the results obtained by the average of the repetitions were reported. To examine the thickness distribution, the formed parts were cut from the blank center up to flange, along a certain path in rolling direction according to Figure 5. The thickness of the different points, by starting from center up to flange, along the marked direction was measured with the increments of 1 mm. A combination of high pressure grease and molybdenum disulphide was used as the lubricant at all temperatures.

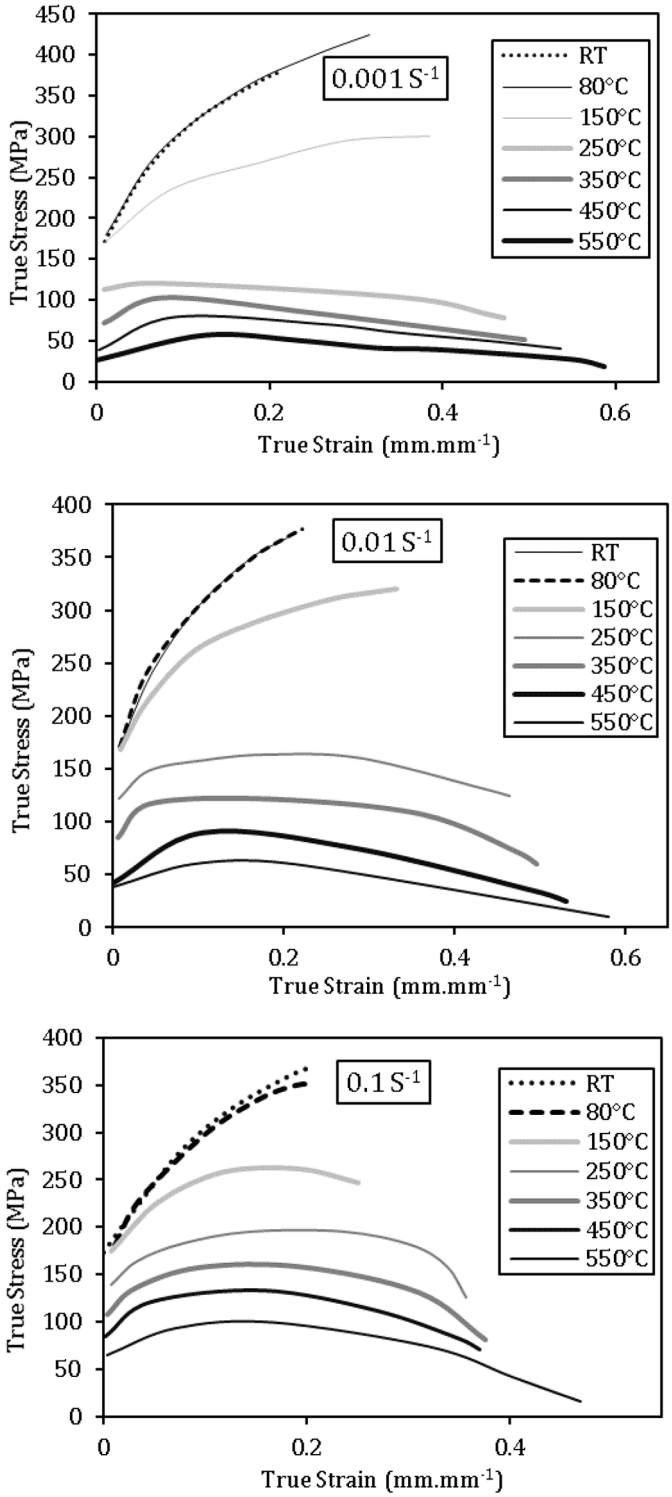


**Fig. 2.** Stress–strain curves at various strain rates.

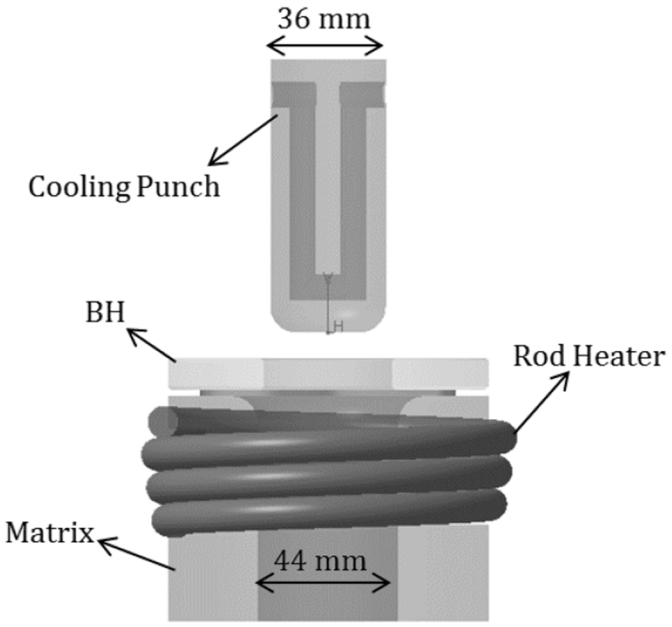


**Fig. 3.** Design of non-isothermal deep drawing tools.

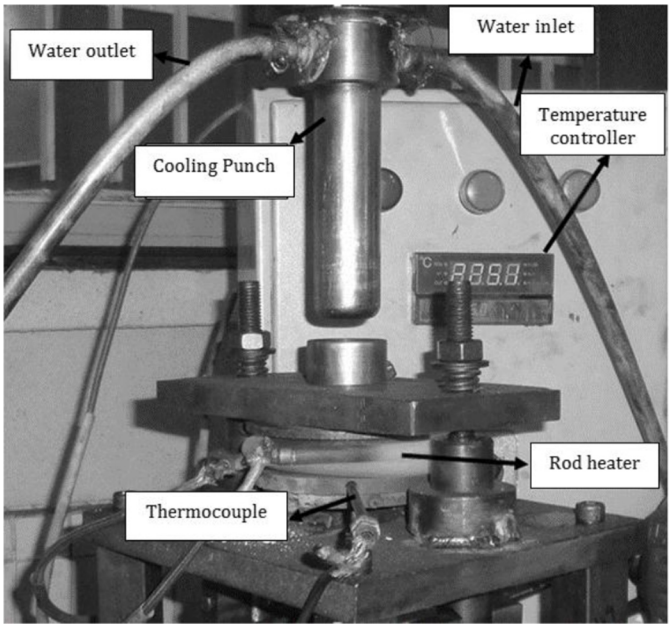


**Fig. 4.** Die setup assembly equipped thermal unit.

## 2.2 Finite elements modelling

Numerical simulations were carried out using ABAQUS\ Explicit Finite Element code. A fully coupled thermo-mechanical analysis was used to evaluate the relationship between nodal temperature values and material properties. As depicted in Figure 6, just one quarter of the tools and the blank were modeled owing to symmetry mode.

In the simulation, both deformation and heat conductions were assumed to be symmetric. The temperature of the tools is assumed to be constant and only the distribution of temperature in the sheet is calculated during simulation.

Tools were modeled with thermal and elastic mechanical properties. The material flow stress of the blank was exerted dependent on strain rate and temperature via uniaxial tension results. The strain-hardening exponent

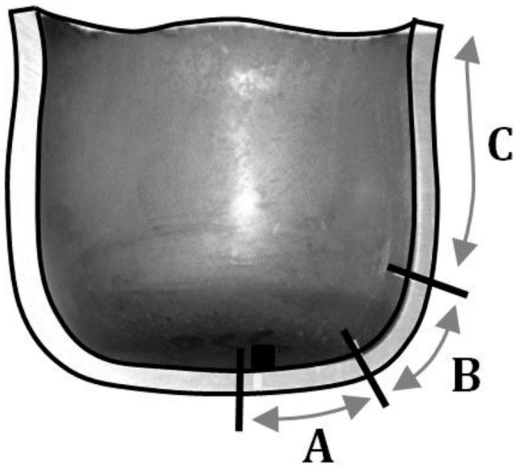


**Fig. 5.** Specimen cut in rolling direction with determined zones.

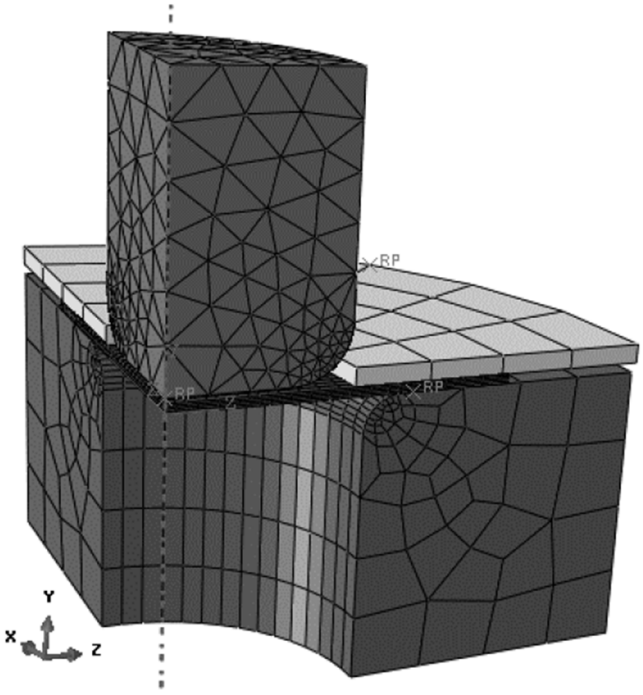


**Fig. 6.** Assembly of tools and blank in finite element model.

($n$-value) and the rate-sensitivity exponent ($m$-value) can be determined using strain-stress curves assuming the Backofen-type constitutive equation (1), as follows:

$$\sigma = C\varepsilon^n \dot{\varepsilon}^m \tag{1}$$

Thermo-physical properties were entered according to Table 2. It may be noted that using temperature dependent thermo-physical properties surely affects the nodal temperature of the formed parts. However, it would be negligible as was ignored by many researchers [7,21–24]. The heat transfer coefficient at tools-blank interface, with dependence on the clearance was applied in 1500 W m$^{-2}$ °C$^{-1}$ [25]. It is worth noting that the material was considered isotropic. Surface-to-surface contact was considered based on Coulomb friction model, in order to determine the friction conditions between the contact surfaces. The numerical values of the BHF and the punch speed were entered according to experimental tests. Since the blank was heated simultaneously with the matrix and blank holder to the set temperature, the initial temperature of the blank was assumed similar to the temperature of the matrix and blank holder. The punch temperature was applied the same as RT. The reduced integration method and hourglass control were employed for the element of type C3D8T, with 8 nodes by both temperature and displacement degrees of freedom. Size of elements is one of the most essential parameters infinite element analysis. To obtain the optimum size and number of elements along the thickness, mesh sensitivity analysis was implemented based on maximum punch load changes. To this end, models with varied element sizes were simulated then their results were studied. According to Figure 7, the results in 4 elements and more along blank thickness, with element length of 1 mm and smaller were converged. Generally, as the number of elements increases and the element size becomes smaller, only the volume of calculations and simulation time may increase, which do not affect the final results.

The mass scaling technique was applied to speed up the computational time with factor equal to 1000, at real step time (due to importance of rate-sensitivity). Figure 8 shows that the ratio of kinetic energy to internal energy is below 10% for the entire simulation time. Hence, the inertial effects due to mass scaling do not sensibly influence the simulation results.

The fracture thickness was investigated for three ruptured parts in order to accurately determine the failure criterion at each temperature. The thickness of the fracture point was 1.6 mm from RT up to 180 °C. It was 1.2 mm for the temperature range from 250 °C to 550 °C. Therefore, the thinning rate more than 20% from RT up to 180 °C, and over 40% from 250 °C up to 550 °C, were considered as failure criteria in finite element model.

## 3 Results and discussion

### 3.1 Effect of forming temperature on initial blank holder force

The minimum value of initial BHF, which can prevent wrinkling of blank, was acquired at various temperatures. It can be noted that too low or too high values for BHF may lead to wrinkles and fracture, respectively. Figure 9 shows the BHF values acquired from experiments with drawing ratio equal to 2, i.e. with 72 mm diameter blanks.

The BHF value does not vary up to 250 °C and is equal to the exerted force at RT. A drop occurs at 300 °C because of work softening resulted from dynamic and recrystallization recovery [26]. Increasing the temperature creates much softer material resulting lower BHF value at 350 °C.

**Table 2.** Physical and thermal properties.

| Material | Density ($kgm^{-3}$) | Young's modulus (GPa) | Poisson's ratio | Specific Heat ($Jkg^{-1}\,°C^{-1}$) | Conductivity ($Wm^{-1}\,°C^{-1}$) |
|---|---|---|---|---|---|
| Tools | 7800 | 210 | 0.3 | 490 | 80 |
| AA5083 | 2700 | 70 | 0.33 | 900 | 120 |

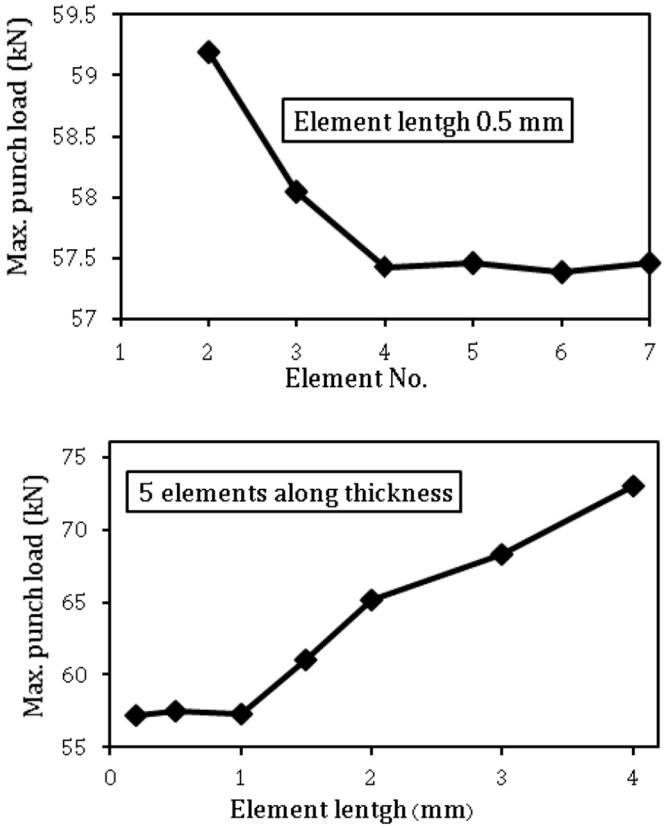


**Fig. 7.** Convergence of numerical maximum forming load in terms of elements size and number.

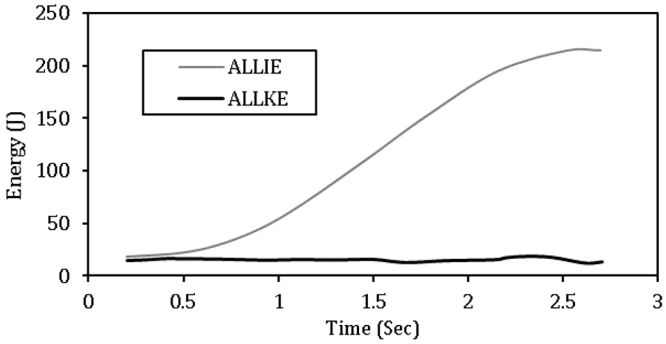


**Fig. 8.** Changes of kinetic energy (ALLKE) and the internal energy (ALLIE).

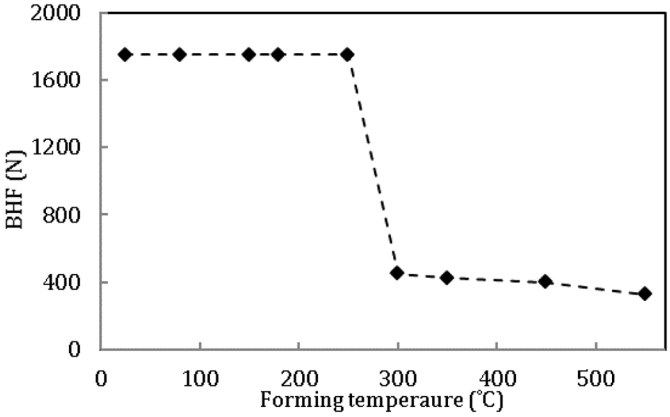


**Fig. 9.** Initial BHF at various temperatures.

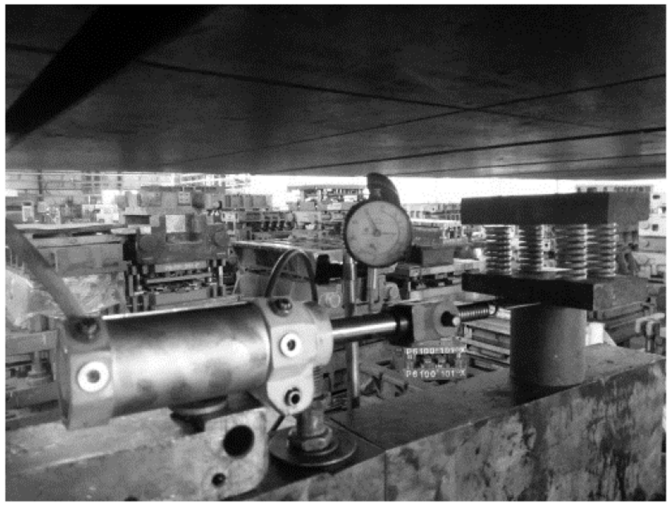

**Fig. 10.** Coulomb friction test setup.

The supperplasticity behavior of AA5083 [27], can intensify the reduction of BHF at 450 °C and 550 °C. The minimum exerted BHF value was 325 N at 550 °C.

### 3.2 Determining the effect of contact friction

In order to find the right friction coefficients inserting in finite element model, Coulomb friction tests were performed at aforementioned forming temperatures, as

**Table 3.** Friction coefficients at speed of 60 mm min$^{-1}$.

| | RT | 80 °C | 150 °C | 180 °C | 250 °C | 350 °C | 450 °C | 550 °C |
|---|---|---|---|---|---|---|---|---|
| Ex. | 0.056 | 0.048 | 0.104 | 0.105 | 0.111 | 0.156 | 0.161 | 0.168 |

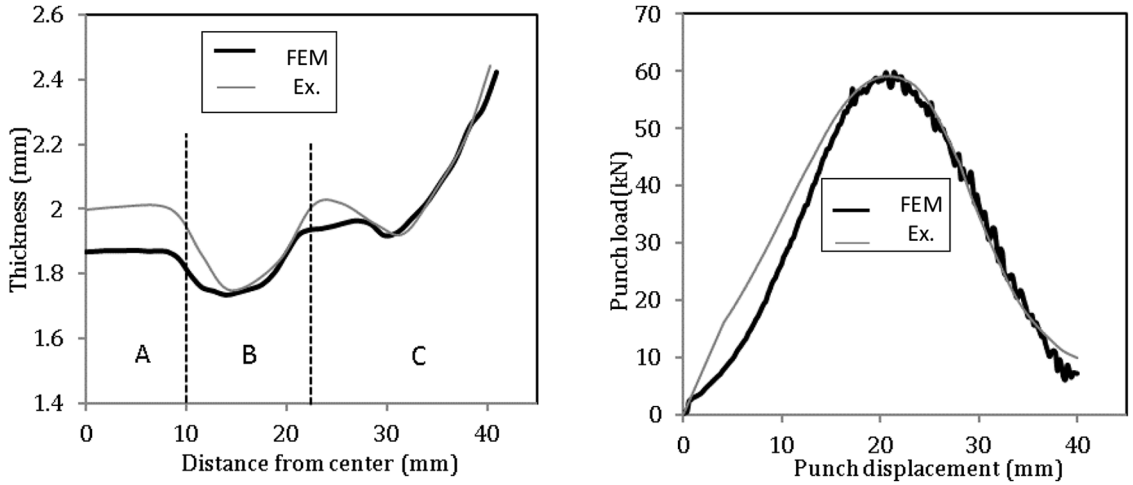


**Fig. 11.** Comparison of experimental and numerical results at speed of 200 mm min$^{-1}$ with blank diameter of 75 mm at 150 °C.

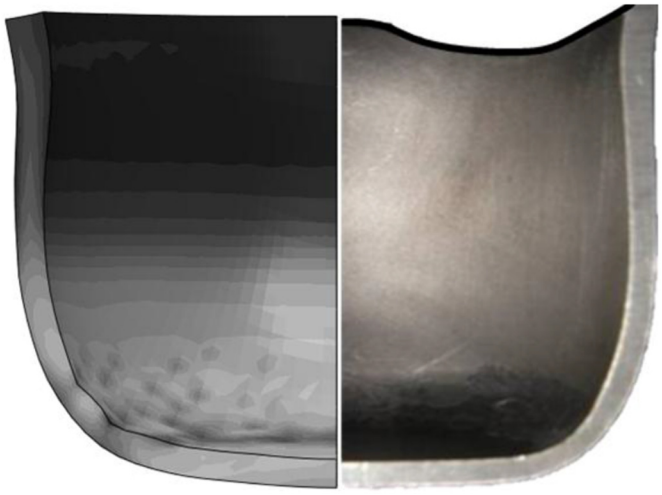

**Fig. 12.** Numerical and experimental formed parts at 150 °C with similar tool radiuses of 8 mm.

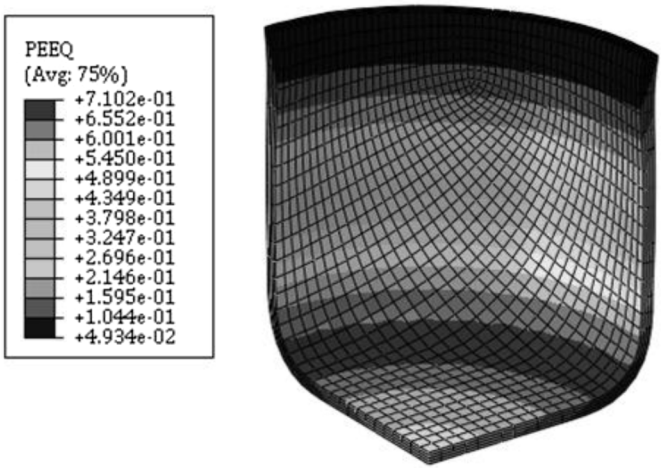


**Fig. 13.** Equivalent Strain (PEEQ) contour for formed part with similar tool radiuses of 6 mm at RT and speed of 378 mm min$^{-1}$.

shown in Figure 10. For each test, the vertical force ($N$) was applied equal to the BHF. Then, the required horizontal force ($F$) to start the blank motion, exerted by a pneumatic cylinder, was measured. Finally, the friction coefficients ($\mu$) were calculated using Coulomb friction law ($F = \mu N$), reported in Table 3.

The comparison of force-displacement curves as well as the thickness distribution at 150 °C are shown in Figure 11. The load changes are fitted exactly, with a low deviation for thickness distribution. In Figure 12, the cut sample is observed in both experiment and numerical model.

### 3.3 The effect of forming temperature on the geometry of the die components

The punch corner radius and the corner radius of the matrix cavity are keys to successful drawing of the blank to create sound parts. Some numerical tests were carried out at RT for different corner radiuses, with the blanks diameter of 75 mm, in order to determine the proper radiuses, which form sound parts. Just one sound part was formed at the same radius equal to 8 mm. At RT, all fractures occurred in the region of contacting with the punch corner radius with the maximum strains exerted to the same region (Fig. 13).

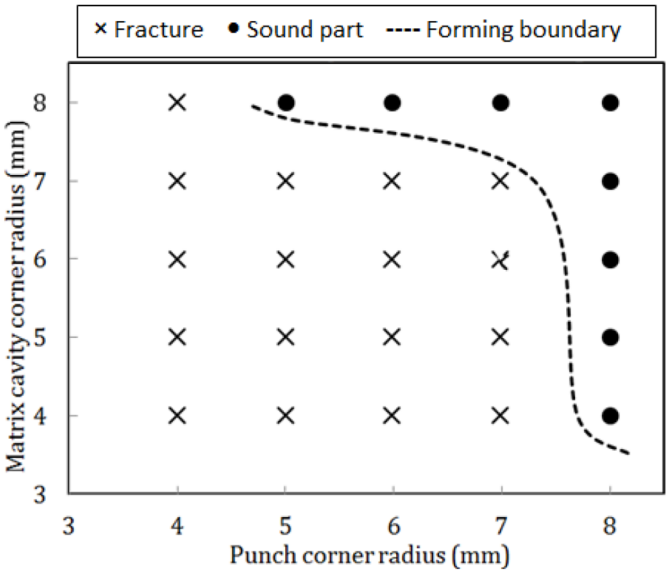


**Fig. 14.** Numerical results for different radiuses at 150 °C.

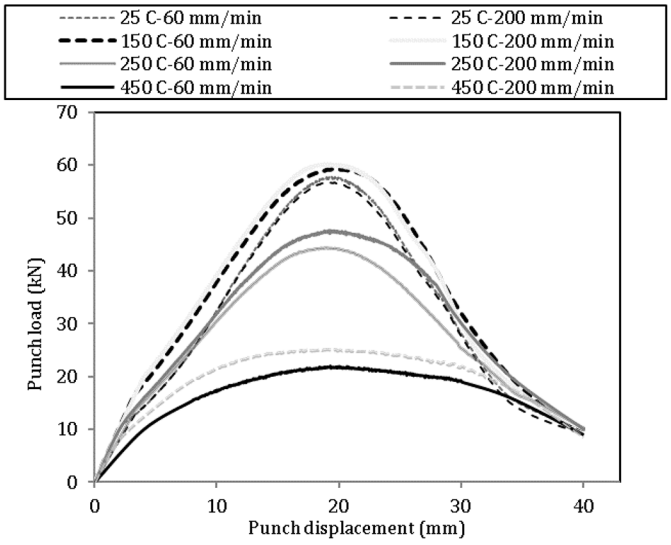


**Fig. 15.** Punch load changes vs. displacement at different temperatures and speeds.

**Table 4.** Numerical results of critical points thinning for different corner radiuses of punch ($R_P$) and matrix cavity ($R_D$).

| $R_P$–$R_D$ (mm) | Thinning rate of critical points |
|---|---|
| 5–8 | 15 |
| 6–8 | 15 |
| 7–8 | 14.5 |
| 8–4 | 14 |
| 8–5 | 12.5 |
| 8–6 | 12.5 |
| 8–7 | 12 |
| 8–8 | 11.5 |

At 150 °C, some numerical tests were performed similarly as RT, to investigate the effect of temperature on values of corner radius (Fig. 14). The points over the dotted line lead to forming of sound parts. It is worth noting that only one sound part was successfully formed in the same values at RT. Formation of more sound parts at 150 °C compared to the RT indicates the ease of material flow at elevated temperatures, which confirms the superiority of the non-isothermal condition to that of the cold deep drawing.

The thinning rate of critical points is reported in Table 4. The tests performing at the corner radiuses of matrix cavity from 4 to 8 mm, with constant value of punch corner radius equal to 8 mm, lead to forming of sound cups. According to Table 4, the thinning rates are reduced by increasing the corner radius of the matrix cavity. The results show that the corner radius of the matrix cavity plays a significant role in forming at 150 °C, and rising its value (at constant punch corner radius), the parts are formed more successfully. According to the numerical results, in order to apply the same geometric conditions to find optimum parameters, other tests were carried out by a punch corner radius of 8 mm, with a corner radius of 8 mm for matrix cavity.

### 3.4 The effect of forming speed on the punch load at different temperatures

The force-displacement changes for parts with the 75 mm diameter are depicted in Figure 15. The maximum force is exerted at the punch displacement about 20 mm. The material flows on the radiuses of the punch and matrix cavity at the initial contact of the punch with the blank. The work hardening enhancement raises the resistance to deformation. Also, the cooling of the blank center exacerbates this increase. In addition, reducing the circumference of the blank in flange region also increases the required load for the forming process. As a result, the required load reaches its maximum value, and then slowly declines by the exiting of the formed part from the free end of the matrix cavity.

It can be seen in Figure 15 that the sensitivity to the strain rate is low at RT. Therefore, increasing the forming speed does not have a noticeable effect on the maximum punch load. By temperature rising to 150 °C, the maximum load increases slightly compared to RT, despite the decrease in material flow stress. This can be justified due to cooling operation. The cooling operation of the blank center (at 150 °C) increases the resistance to deformation, thus raises the strength of the blank center. The resistance rise of the blank center caused by the cooling operation dominates the reduction of blank strength at 150 °C. This strength enhancement results in an increase in the maximum punch load relative to the RT. The speed

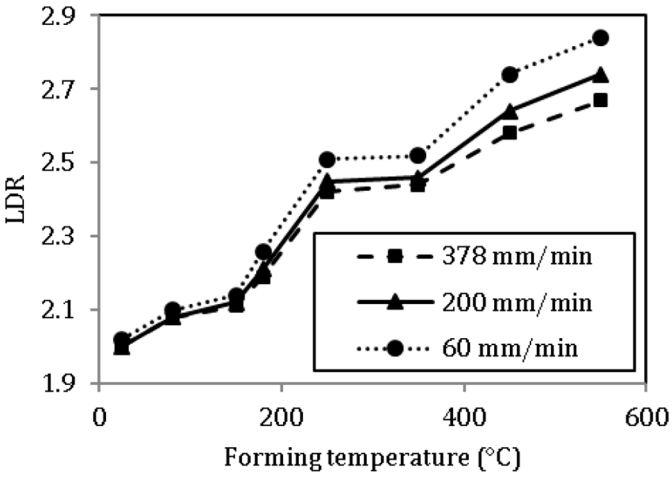


**Fig. 16.** Numerical results of LDRs at different forming temperatures and speeds.

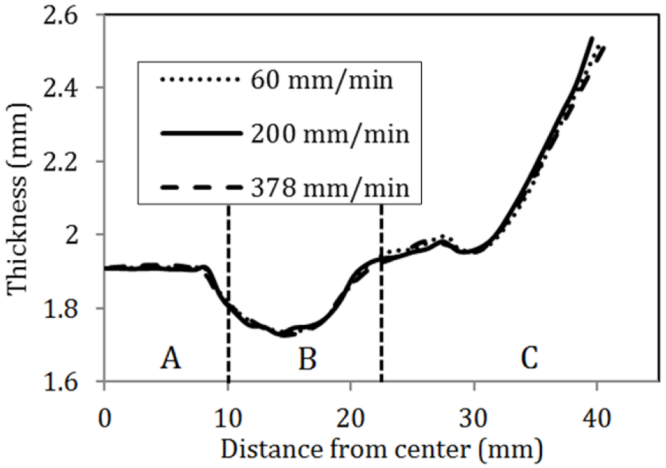


**Fig. 17.** Numerical thickness distribution for different speeds at RT.

increase from 60 to 200 mm min$^{-1}$ leads to a reduction in the process time at 150 °C. As a result, the blank is cooled down over a shorter period of time. Therefore, the strength does not increase much, thus the punch maximum load is reduced. Additionally, the higher strain rate obtained from the higher speed brings about an increase in the strain-hardening exponent, requiring higher forming loads. Therefore, at this temperature (150 °C), an increase around 1 kN at maximum forming load was created at 200 mm min$^{-1}$ compared to 60 mm min$^{-1}$. By temperature increasing to 250 °C, the blank strength significantly decreases, possibly due to the initiation of the dynamic recovery. This significant reduction at elevated temperatures overcomes the strength enhancement caused by the cooling operation, and leads to a sharp reduction in forming load (Fig. 15). At 250 °C, the increase in the deformation resistance at high strain rates, created an increase equal to 3 kN in the maximum forming load at 200 mm min$^{-1}$ compared to a 60 mm min$^{-1}$. A similar trend in strain was reported by Naka et al [6,28]. The strength reduction of material was exacerbated in hot condition at temperatures above 400 °C, whereas the maximum forming load at 450 °C with the speed equal to 60 mm min$^{-1}$ declined about 63% and 50% compared to 150 °C and 250 °C respectively. At this temperature (450 °C) with the speed of 200 mm min$^{-1}$, an increase of about 13% was created at the maximum forming load relative to 60 mm min$^{-1}$, while this increase in the maximum forming load, due to the increase in the speed, was approximately 7% at 250 °C.

### 3.5 The effect of forming speed on limiting drawing ratio at various temperatures

Figure 16 shows the numerical LDRs at various speeds and temperatures. In all tests, the trend of changes is similar. The various speeds up to 150 °C had a slight effect on the LDR. The effect of the strain rate on the rate-sensitivity exponent is increased by rising the temperature, consequently lower rates create smaller strains. Therefore, the

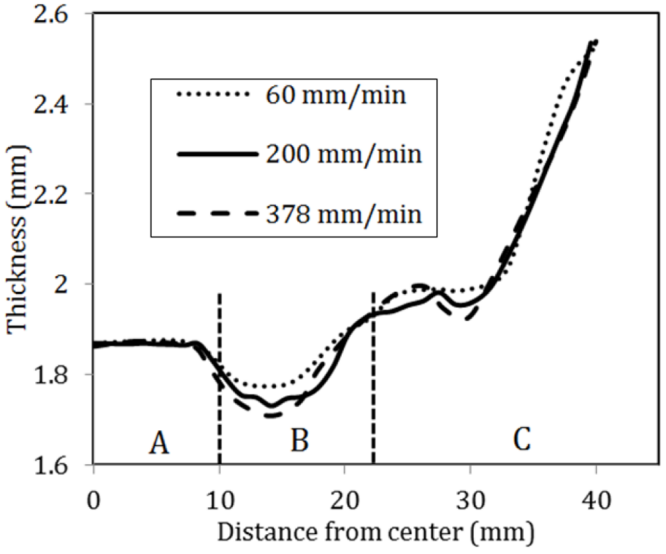


**Fig. 18.** Numerical thickness distribution for different speeds at 150 °C.

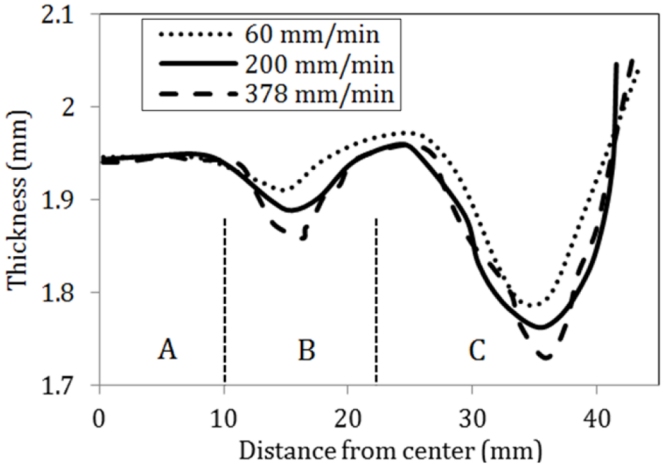


**Fig. 19.** Numerical thickness distribution for different speeds at 450 °C.

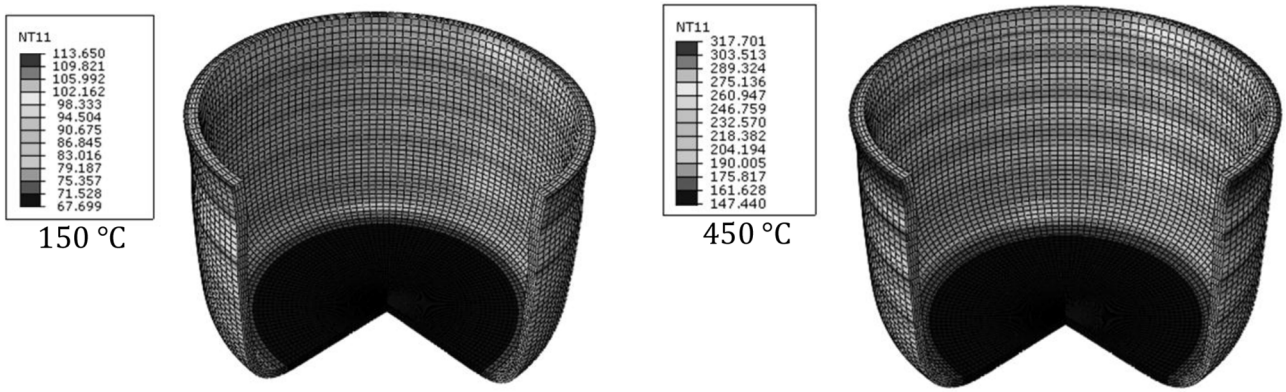


**Fig. 20.** Nodal temperature (NT11) contour at 378 mm min$^{-1}$.

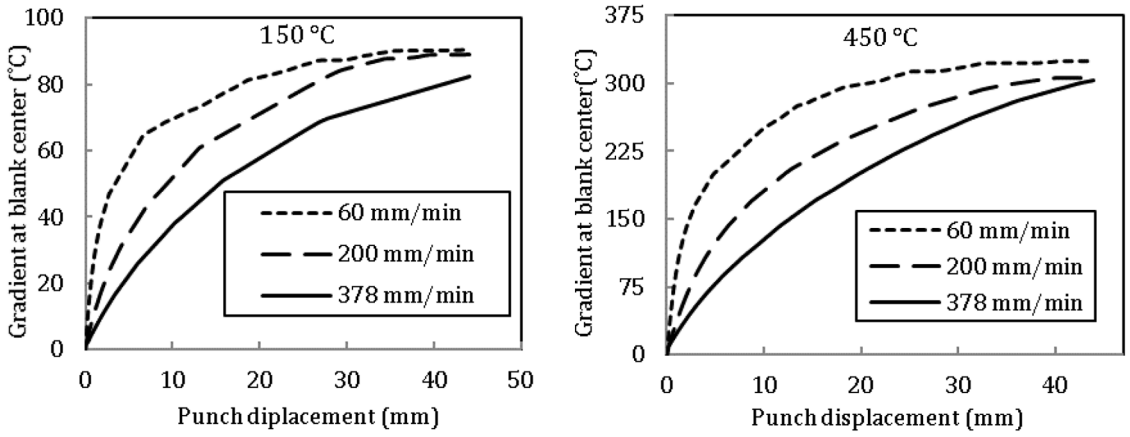


**Fig. 21.** Numerical results of temperature gradient changes for different speeds at blank center.

possibility of achieving higher drawing ratios grows, which is in good agreement with the results of [29,30]. As discussed, the strain rate has a significant influence on the rate-sensitivity exponent at temperatures over 400 °C. Therefore, lower speeds create greater increase in drawing ratios at temperatures over 400 °C. The higher rise in diagram slope at speed of 60 mm min$^{-1}$ confirms this issue. It should be pointed out that the escalating trend of the LDR variations up to hot temperatures can be originated from the superplasticity behavior, which was not previously reported for some aluminum grades [25,31–33].

In order to study the effect of forming speed on thickness distribution, some parts were analyzed at three forming speeds and three different temperatures using finite element model. The thickness distributions of the formed parts are depicted in Figures 17–19. At RT, increasing the forming speed does not control the thickness distribution and critical points (points with the minimum thickness) due to low sensitivity to strain rates. At 150 °C, the higher sensitivity of strain rate compared to RT, results in a slight enhancement of the thinning ratio of critical points, as shown in Figure 18. On the other hand, large rate-sensitivity exponent at 450 °C has a tangible effect on thickness distribution as depicted in Figure 19. The faster the forming speed is, the more uniform the thickness distribution becomes. As Naka et al. [6] reported, the rate-sensitivity exponent is dramatically affected by low strain rates at temperatures above 300 °C. Hence, the drop in the thinning ratio of critical points at lower speeds can be justified due to large rate-sensitivity exponent and grain boundary sliding at 450 °C [34,35].

### 3.6 The effect of forming speed on temperature gradient at different temperatures

Three parts were investigated numerically at three speeds and two different temperatures, to investigate the effect of temperature and speed on the temperature gradient at blank center. As stated, the initial temperature for blank, blank holder, and matrix was applied equally in finite element model. The regions of the blank in contact with the punch cool down much rapidly, when compared to other regions. In the beginning of the process, the blank center is continuously in contact with the cooling punch hence the maximum temperature reduction occurs at the bottom of the cup (zone A), as shown in Figure 20. Moreover, at the end of the process, the temperature of the blank center at 150 °C and 450 °C are 67 °C and 147 °C, indicating 55% and 67% decline in initial temperature, respectively. This sensible decrease justifies the strength enhancement of the blank center, particularly the region in contact with the punch corner radius. Consequently, the possibility of

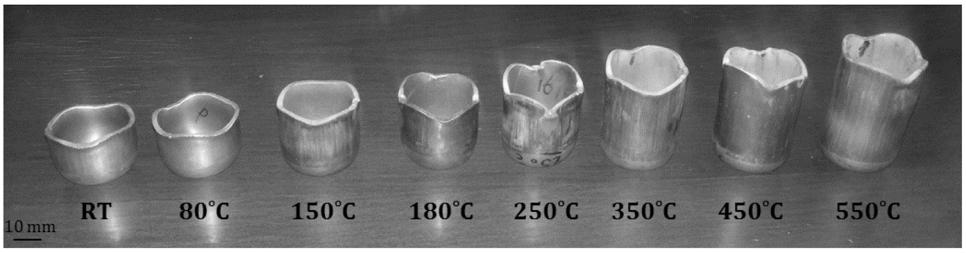


**Fig. 22.** Earing behavior at the free end of the formed parts for different temperatures.

achieving higher drawing ratios in the non-isothermal condition is increased compared to the isothermal one, as previously reported [33,36,37].

The decline in temperature of the blank center obtained by cooling punch creates a temperature gradient between the blank center and the flange region. By increasing the forming speed and thus reducing the process time, the contact time of the blank with the punch is reduced. Therefore, the cooling operation is performed at a lower rate. As a result, the temperature of the blank center at the end of the process faces lower decrease for higher speeds, which eventually reduces the temperature gradient (Fig. 21). The Lower reduction in temperature of blank for higher speeds increases the resistance to deformation and hence reduces the drawing ratios at higher speeds, as shown in Figure 16. Based on numerical results, at the lowest exerted forming speed equal to 60 mm min$^{-1}$, the temperature gradient at the end of the process for temperatures equal to 150 °C and 405 °C are respectively 90 °C and 325 °C, which show an increase about 10% and 8% compared to speed of 378 mm min $^{-1}$, respectively. This increase is lies at the root of less time-consuming contact of the blank with the punch, and hence the less intense cooling operation at higher speeds.

### 3.7 Investigating the earring behavior at different temperatures

In Figure 22, it can be seen that the earring profile of the cups is formed with four peaks in the directions of ±45 °, and four valleys in the direction of rolling and perpendicular to it for all temperatures. According to the theoretical results of Hosford and Caddell [19], the formation of peaks in the directions of ±45 ° indicates that the value of $r_{45}$ should be greater than the two other values, i.e. $r_0$ and $r_{90}$. Therefore, a negative value is produced for planar anisotropy according to equation (2) ($\Delta R < 0$). This negative value was also reported for aluminum 5083 [38,39].

$$\Delta R = \frac{R0 + R90 - 2\,R45}{2} \tag{2}$$

The heights of the peaks are gradually decreased by increasing the temperature up to warm condition, then decreases more intensely for hot range, as depicted in Figure 23. Since by raising the temperature the anisotropy parameters ($r_i$) often increase for aluminum alloys, and nears to the value equal to 1, thus the material shows a great tendency to be anisotropic [10,40]. Consequently, increasing r values leads to the decrease in the peaks height for elevated temperatures. The increase in $r$ values and approaching the value of 1 (because of temperature increase) creates planar strains and results in more resistance to the thickness reduction. The resistance to the thickness reduction is a justification to delay in failure. Consequently, improved formability and higher drawing ratios are expected. Despite the

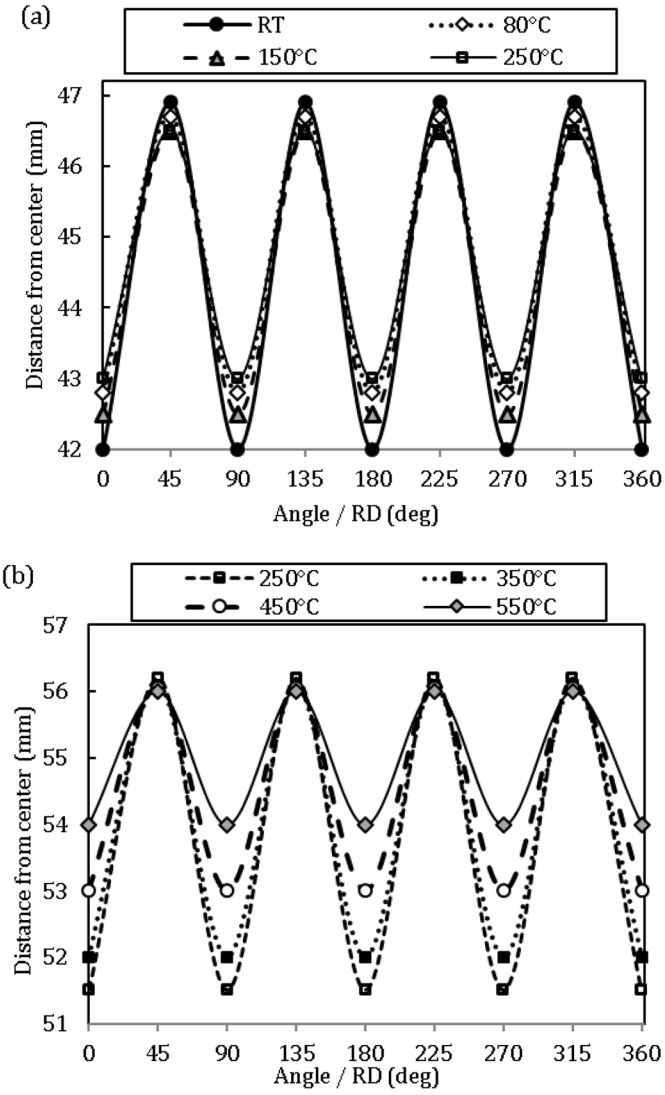


**Fig. 23.** Earing profiles for different temperatures at 378 mm min $^{-1}$ for (a) formed parts with 75 mm blank diameter at RT-250 °C and (b) formed parts with 83 mm blank diameter at 250–550 °C

increasing $r$ values at elevated temperatures, the $r_{45}$ value is still greater than two other $r$ values. As a result, the position of the ears does not change by increasing the temperature, and still has four ears in the direction of $\pm 45$ ° at all temperatures.

## 4 Conclusion

The effects of temperature and forming speed on the punch load, thickness distribution, and earing behavior, as well as limiting drawing ratio and temperature gradient were investigated for AA5083 non-isothermal hot deep drawn parts. The main findings are summarized as follows:

- The corner radius of the matrix cavity plays a key role at 150 °C, while increasing its value (at the constant punch corner radius) decreases the thinning rate of critical points. As a result, the thickness distribution is improved and the cups are formed more successfully.
- The cooling operation of the blank center at 150 °C increases the resistance to the deformation, and thus causes a strength enhancement of the blank material, which ultimately leads to an increase in the maximum punch load, compared to the room temperature. A sharp drop is created in the punch load by increasing the temperature to 250 °C. At 450 °C, the maximum punch load at speed of 60 mm min $^{-1}$ is about 63% lower than the temperature of 150 °C, and about 50% lower than the temperature of 250 °C.
- By reducing the speed at temperatures over 150 °C, the limiting drawing ratio increases and the thickness distribution improves. These changes occur more intensely at temperatures above 400 °C, with the advent of the superplasticity behavior.
- Despite the decrease in ears height, the number (4) and the position of the ears ($\pm 45$ °) are constant while increasing the temperature.

The author would like to thank the support of Iran Khodro Advanced Dies Co. for supplying part of the experimental equipment utilized in the Coulomb friction test setup (grant No. S-1192).

## References

[1] S. Kalpakjian, S.R. Schmid, C.-W. Kok, Manufacturing Processes for Engineering Materials, Pearson, Prentice Hall, 2008

[2] N.H. Kacem, N. Haddar, R. Elleuch, Failure analysis of an automotive shock absorber cup during manufacturing process, Mech. Ind. **17**, 604 (2016)

[3] R. Boissiere, P. Vacher, J. Blandin, Scale factor and punch shape effects on the expansion capacities of an aluminum alloy during deep-drawing operations, Mech. Ind. **15**, 159–166 (2014)

[4] T. Naka, F. Yoshida, Deep drawability of type 5083 aluminium-magnesium alloy sheet under various conditions of temperature and forming speed, J. Mater. Process. Technol. **89**, 19–23 (1999)

[5] Y. Moon, Y. Kang, J. Park, S. Gong, Tool temperature control to increase the deep drawability of aluminum 1050 sheet, Int. J. Mach. Tools Manuf. **41**, 1283–1294 (2001)

[6] T. Naka, G. Torikai, R. Hino, F. Yoshida, The effects of temperature and forming speed on the forming limit diagram for type 5083 aluminum-magnesium alloy sheet, J. Mater. Process. Technol. **113**, 648–653 (2001)

[7] H. Takuda, K. Mori, I. Masuda, Y. Abe, M. Matsuo, Finite element simulation of warm deep drawing of aluminium alloy sheet when accounting for heat conduction, J. Mater. Process. Technol. **120**, 412–418 (2002)

[8] H. Wang, Y.-B. Luo, P. Friedman, M.-H. Chen, L. Gao, Warm forming behavior of high strength aluminum alloy AA7075, Trans. Nonferrous Met. Soc. China **22**, 1–7 (2012)

[9] X. Chu, L. Leotoing, D. Guines, E. Ragneau, Temperature and strain rate influence on AA5086 Forming Limit Curves: experimental results and discussion on the validity of the M-K model, Int. J. Mech. Sci. **78**, 27–34 (2014)

[10] M. Ghosh, A. Miroux, R. Werkhoven, P. Bolt, L. Kestens, Warm deep-drawing and post drawing analysis of two Al-Mg-Si alloys, J. Mater.Process. Technol. **214**, 756–766 (2014)

[11] H. Laurent, J. Coër, P. Manach, M. Oliveira, L. Menezes, Experimental and numerical studies on the warm deep drawing of an Al-Mg alloy, Int. J. Mech. Sci. (2015)

[12] M.H. Cetin, A. Ugur, O. Yigit, H. Gokkaya, E. Arcaklioglu, Development of forming temperature curves for warm deep drawing process under non-isothermal conditions, Arab. J. Sci. Eng. **40**, 2763–2784 (2015)

[13] J. Noder, S. DiCecco, C. Butcher, M. Worswick, Finite element simulation of non-isothermal warm forming of high-strength aluminum alloy sheet, AIP Conf. Proc. **1**, 080017 (2017)

[14] J. Noder, A. Abedini, T. Rahmaan, S. DiCecco, C. Butcher, M. Worswick, An Experimental and Numerical Investigation of Non-isothermal Cup Drawing of a 7XXX-T76 Aluminum Alloy Sheet, IOP Conf. Ser. Mater. Sci. Eng. **1**, 012019 (2018)

[15] T. Pepelnjak, E. Kayhan, B. Kaftanoglu, Analysis of non-isothermal warm deep drawing of dual-phase DP600 steel, Int. J. Mater. Form. 1–18 (2018)

[16] S. Kurukuri, A.H. van den Boogaard, M. Ghosh, A. Miroux, Thermo-mechanical Forming of Al-Mg-Si Alloys: Modeling and Experiments, AIP Conf. Proc. **1**, 810–817 (2010)

[17] D.G. Tari, M. Worswick, S. Winkler, Experimental studies of deep drawing of AZ31B magnesium alloy sheet under various thermal conditions, J. Mater. Process. Technol. **213**, 1337–1347 (2013)

[18] A. Barimani Varandi, S. Jamal Hosseinipour, Investigation of process parameters in production of cylindrical parts by gradient warm deep drawing, Modares Mech. Eng. **14** (2015)

[19] W.F. Hosford, R.M. Caddell, Metal Forming: Mechanics and Metallurgy, Cambridge University Press, Cambridge, 2011

[20] L.D. Hefti, Commercial airplane applications of superplastically formed AA5083 aluminum sheet, J. Mater. Eng. Perform. **16**, 136–141 (2007)

[21] S. Kaya, Nonisothermal warm deep drawing of SS304: FE modeling and experiments using servo press, Int. J. Adv. Manuf. Technol. **83**, 1047–1056 (2016)

[22] M. Steffensen, J. Danckert, Finite Element Simulation Of Magnesium AZ31 Alloy Sheet In Warm Hydroforming, AIP Conf. Proc. **1**, 551–556 (2007)

[23] H. Takuda, K. Mori, T. Masachika, E. Yamazaki, Y. Watanabe, Finite element analysis of the formability of an austenitic stainless steel sheet in warm deep drawing, J. Mater. Process. Technol. **143**, 242–248 (2003)

[24] K. Shinagawa, K.-I. Mori, K. Osakada, Finite element simulation of deep drawing of stainless steel sheet with deformation-induced transformation, J. Mater. Process. Technol. **27**, 301–310 (1991)
[25] G. Palumbo, L. Tricarico, Numerical and experimental investigations on the warm deep drawing process of circular aluminum alloy specimens, J. Mater. Process. Technol. **184**, 115–123 (2007)
[26] Y. Ding, K. Gao, S. Guo, S. Wen, H. Huang, X. Wu, Z. Nie, D. Zhou, The recrystallization behavior of Al-6Mg-0.4 Mn-0.15 Zr-xSc (x= 0.04–0.10 wt%) alloys, Mater. Charact. **147**, 262–270 (2019)
[27] S. Hosseinipour, An investigation into hot deformation of aluminum alloy 5083, Mater. Des. **30**, 319–322 (2009)
[28] C.R. Alavala, High temperature and high strain rate superplastic deep drawing process for AA2618 alloy cylindrical cups, Int. J. Sci.Eng. Appl. Sci. **2**, 35–41 (2016)
[29] M. Türköz, D. Acar, M. Dilmeç, H.S. Halkaci, Investigation on the optimal geometrical parameters for cylindrical cups in warm hydromechanical deep drawing process, Mechanical and Aerospace Engineering (ICMAE), 2017 8th International Conference on. IEEE, 2017 155–159
[30] H. Laurent, J. Coër, P. Manach, M. Oliveira, L. Menezes, Experimental and numerical studies on the warm deep drawing of an Al-Mg alloy, Int. J. Mech. Sci. **93**, 59–72 (2015)
[31] W. Hui, Y.-b. Luo, P. Friedman, M.-h. Chen, G. Lin, Warm forming behavior of high strength aluminum alloy AA7075, Trans. Nonferrous Met. Soc. China **22**, 1–7 (2012)
[32] H.S. Kim, A combined FEA and design of experiments approach for the design and analysis of warm forming of aluminum sheet alloys, Int. J. Adv. Manuf. Technol. **51**, 1–14 (2010)
[33] G. Ambrogio, L. Filice, G. Palumbo, S. Pinto, Prediction of formability extension in deep drawing when superimposing a thermal gradient, J. Mater. Process. Technol. **162**, 454–460 (2005)
[34] E. Sato, H. Masuda, Y. Sugino, S. Ukai, Local Accommodation Processes of Superplastic Grain Boundary Sliding: Their Direct Observation in Two-Dimensional Grain Boundary Sliding, Defect Diffus. Forum **385**, 155–160 (2018)
[35] K.A. Babu, V.S. Sarma, C. Athreya, K. Padmanabhan, Experimental verification of grain boundary-sliding controlled steady state superplastic flow in both continually and statically recrystallizing Al alloys, Mater. Sci. Eng. **657**, 185–196 (2016)
[36] G. Palumbo, D. Sorgente, L. Tricarico, S. Zhang, W. Zheng, Numerical and experimental investigations on the effect of the heating strategy and the punch speed on the warm deep drawing of magnesium alloy AZ31, J. Mater. Process. Technol. **191**, 342–346 (2007)
[37] S. Yoshihara, H. Yamamoto, K. Manabe, H. Nishimura, Formability enhancement in magnesium alloy deep drawing by local heating and cooling technique, J. Mater. Process. Technol. **143**, 612–615 (2003)
[38] H. Tanaka, Y. Nagai, Y. Oguri, H. Yoshida, Mechanical properties of 5083 aluminum alloy sheets produced by isothermal rolling, Mater. Transac. **48**, 2008–2013 (2007)
[39] M. Janbakhsh, M. Riahi, F. Djavanroodi, Anisotropy Induced Biaxial Stress-Strain Relationships in Aluminum Alloys, Int. J. Adv. Des. Manuf. Technol. **5**, 1 (2012)
[40] M. Tajally, E. Emadoddin, Mechanical and anisotropic behaviors of 7075 aluminum alloy sheets, Mater. Des. **32**, 1594–1599 (2011)

**Cite this article as**: A.B. Varandi, The non-isothermal hot deep drawing of AA5083 aluminum alloy, Mechanics & Industry **21**, 112 (2020)